Nashimoto and Yokoo
Earth, Planets and Space (2023) 75:57
https://doi.org/10.1186/s40623-023-01786-8

Earth, Planets and Space

TECHNICAL REPORT

Open Access

A new method to reconstruct the 3D ground surface temperature from aerial TIR and visible images: application to the active crater of Aso volcano, Japan

Subaru Nashimoto[1] and Akihiko Yokoo[2*]

Abstract

At active volcanoes, the surface temperature and its spatial distribution can indicate changes in the underlying magmatic and hydrothermal system. Surface temperature monitoring has been widely performed using thermal remote sensing with thermal infrared (TIR) cameras. One of the drawbacks of this method is that the unknown viewing orientation of TIR images inhibits quantitative evaluations of the spatial extent and distributions of thermal anomalies. Therefore, many studies have performed 3D temperature-field reconstructions by processing TIR images photogrammetrically. However, these studies have not included the correction of TIR wave atmospheric attenuation and viewing-angle variation in emissivity in the reconstruction procedure, which can result in significant temperature misestimation. We propose a simple method that incorporates the correction into the reconstruction process, which can improve the estimation of surface temperature, especially in rugged terrains. We demonstrate our method for the active crater of Aso volcano in Japan. We create digital elevation models by applying the Structure from Motion–Multi-view Stereo algorithm to aerial visible images taken at the same time as the TIR images and then project the TIR images onto the DEM with the direct georeferencing method. The correction is carried out using the geometric parameters acquired in the process. We create 1-m resolution orthorectified thermal images of the crater on two separate dates (18 August 2020 and 16 March 2022) and calculate the heat discharge rates from steaming grounds and a volcanic lake. We find that the heat discharge rate from the fumarolic field on the south crater wall showed a sevenfold increase after the phreatic explosions that occurred on 14 and 20 October 2021.

Keywords Thermal remote sensing, Unoccupied aerial vehicle, Direct georeferencing, Orthorectified thermal image, Aso volcano, Heat discharge rate

*Correspondence:
Akihiko Yokoo
yokoo.akihiko.5a@kyoto-u.ac.jp
Full list of author information is available at the end of the article

Graphical Abstract

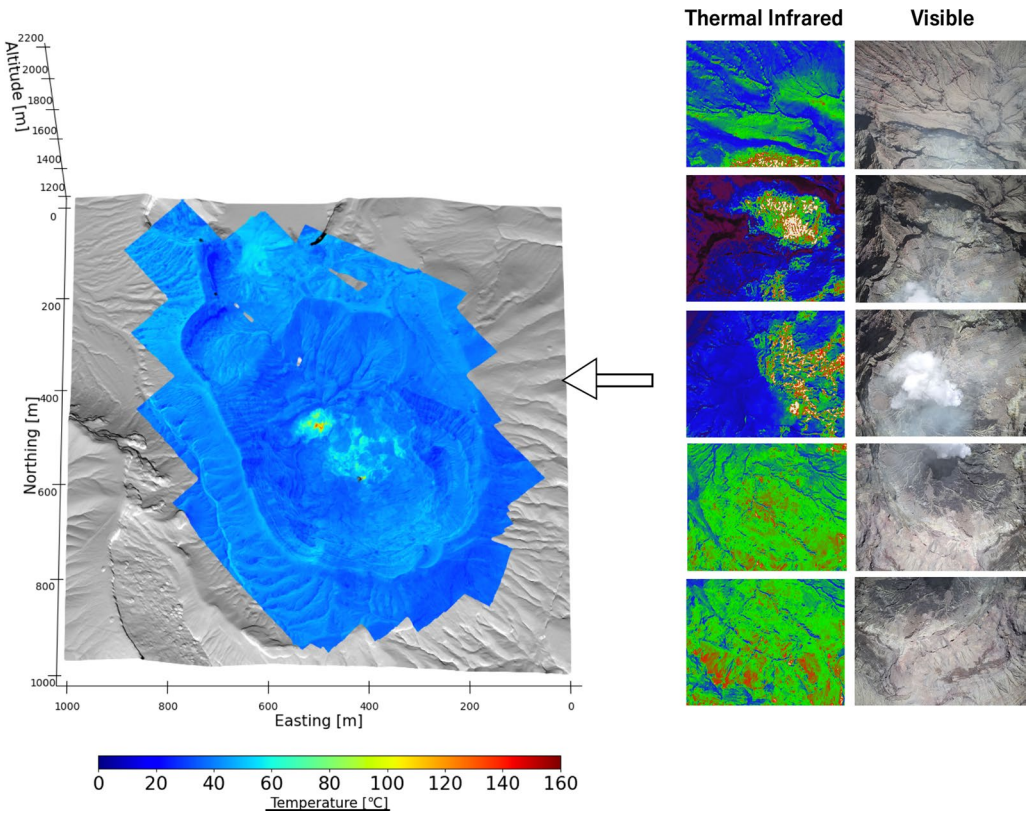

Introduction

At active volcanoes, monitoring changes in the surface temperature and spatial distribution, such as temperature increases in fumarolic vents or extension of thermal anomalies, is crucial, because they are often associated with activation of underlying hydrothermal or magmatic systems. At Campi Flegrei in Italy, Chiodini et al. (2007) discovered that some fumarolic vents exhibited anomalous temperature increases before and after two seismic swarms. This increase was due to hydrothermal fluid transfer from a deeper part of the hydrothermal system to the fumarole field. At Satsuma–Iwojima volcano, Japan, Matsushima et al. (2003) observed that high-temperature anomalies migrated from the peripheral zone of the summit crater to its center as a sizable degassing vent appeared in the crater. It was concluded that the ascent of the magma head to the shallow part of the volcano caused this phenomenon.

Surface temperature measurements for active volcanoes have been obtained by satellite, airborne, and ground-based remote sensing, as well as by traditional in situ temperature acquisition with thermometers. In recent years, thermal infrared (TIR) cameras have been used extensively for volcano monitoring, because they enable seamless temperature data acquisition over broad areas. Their application includes hot crack detection (Bonaccorso et al. 2003), estimation of heat flux discharged from steaming grounds (Sekioka and Yuhara 1974; Gaudin et al. 2013) and observation of lava dome emplacement (Vaughan et al. 2005).

Despite their widespread use, there are two problems with TIR camera observations. One problem is that it is challenging to associate TIR images of target objects in certain locations with world coordinates (georeferencing), especially for ground-based observations. Georeferencing of TIR images is essential to quantitatively evaluate the spatial extent or distribution of thermal anomalies. The difficulty is attributed to highly oblique and unknown viewing orientations (Lewis et al. 2015). The other problem is that the apparent temperature acquired with TIR cameras contains errors that originate from several factors. Water vapor and volcanic gases in the atmosphere can significantly affect temperature data through the attenuation of TIR waves (Sawyer and Burton 2006). The emissivity of the target object can also be an important factor. The surfaces of volcanic fields are

not perfect black bodies. Therefore, we must correct the temperature data considering the effects of emissivity, which vary depending on the roughness of the surface and the viewing angle (Ball and Pinkerton 2006).

Previous studies have addressed these two problems using the following approaches. For georeferencing of TIR images, some studies employed photogrammetric strategies: monoplotting (James et al. 2006; Fornaciai et al. 2021) and the Structure from Motion–Multi-view Stereo (SfM–MVS) algorithm (Lewis et al. 2015; Thiele et al. 2017; Lewis et al. 2020). Concerning the atmospheric attenuation of TIR waves, Stevenson and Varley (2008) corrected the temperature data of TIR images using an atmospheric transmission model. Ball and Pinkerton (2006) experimentally determined the relationship between the viewing angle and emissivity of an Etnean lava sample. Using this relationship, Yokoo and Ishii (2021) corrected the data extracted from the TIR images of a fumarolic field at Aso volcano in Japan.

Although much effort has been made to mitigate the effect of atmospheric attenuation and emissivity, few studies have focused on the effects of the variable viewing distance and viewing angle over a single TIR image. These effects cannot be disregarded, especially on steep and complex terrains in volcanic environments (Additional file 1: Figs. S1, S2, S3). James et al. (2006) addressed this issue at Etna volcano, Italy. They calculated the viewing distance for each pixel using a digital elevation model (DEM) and viewing orientation acquired through georeferencing. Then, a pixelwise correction was performed using an atmospheric attenuation correction code. Although James et al. (2006) succeeded in the pixelwise correction of atmospheric attenuation, they did not consider the viewing-angle dependence of emissivity.

In this paper, we propose a new simple TIR data processing method to simultaneously achieve georeferencing and pixelwise correction of the effects of atmospheric attenuation and the viewing angle dependency of emissivity. Our method aims to create orthorectified thermal images of volcanoes by georeferencing many corrected TIR images. We employed the direct method (Correia et al. 2022) for georeferencing. We corrected temperature data using techniques reviewed by Yokoo and Ishii (2021). These pixelwise corrections have become possible thanks to discussions on the online Forum of ExifTools and Minkina and Dudzik (2009). They discovered a technique to extract signal data from TIR images acquired with FLIR Inc. cameras, conversion formulas of the signal data and atmospheric correction formulas within FLIR's cameras. We demonstrated the method at the active crater of Aso volcano and created two orthorectified thermal images in August 2020 and March 2022.

Aso volcano is one of the most active volcanoes in Japan. Its volcanic activities have been focused only in the northern crater of the Nakadake stratocone (Additional file 1: Fig. S4) since the 1940s (Sudo et al. 2006). The most recent magmatic activity of the crater started in July 2019 during which sporadic ash emissions continued until June 2020 (Miyabuchi et al. 2021). A relatively quiescent period with fumarolic activity followed the eruptive period. On 14 and 20 October 2021, small phreatic explosions occurred. The explosion on 20 October generated a pyroclastic density current that ran down 1.6 km from the crater and devastated the area around it. Since the entry to the proximal area had been prohibited under regulations issued a week before in response to intensification of its volcanic activities, the explosions caused no causalities. The explosions left a high-temperature crater lake on the crater floor, and at the time of writing (December 2022), no eruptions had occurred since October 2021.

Methods

Data acquisition

We performed airborne thermal surveys on 18 August 2020 and 16 March 2022 at the active crater of Aso volcano (2020 and 2022 surveys, respectively). Clear days were chosen for our surveys to minimize the effects of condensed vapor discharged from fumaroles in the crater. We used a TIR camera (FLIR Zenmuse XT2) mounted on an Unoccupied Aereal Vehicle (UAV; DJI Matrice 200). We used two XT2 models, one with a 9 mm focal length for the 2020 survey and the other with a 13 mm focal length for the 2022 survey. These TIR cameras can acquire both visible and TIR images of the same scene in one shot (Fig. 1a, b). The resolution of visible images was 4000×3000 pixels and that of TIR cameras was 360×256 pixels (2020 survey) and 640×540 pixels (2022 survey). We kept a constant flight height of 150 m above the crater rim, thereby maintaining the consistency of the ground sample distance (GSD: the distance between the centers of two adjacent pixels on a target surface) on the crater floor. The GSDs of the TIR images were approximately 20 cm and 15 cm at the crater rim and 50 cm and 30 cm at the crater floor in the 2020 and 2022 surveys, respectively. We took 755 and 922 sets of overlapping visible and TIR images in 2020 and 2022, respectively. The image acquisition positions are shown in Fig. 2.

Data processing

The workflow of the proposed method is illustrated in Fig. 3. We built DEMs from only the visible image

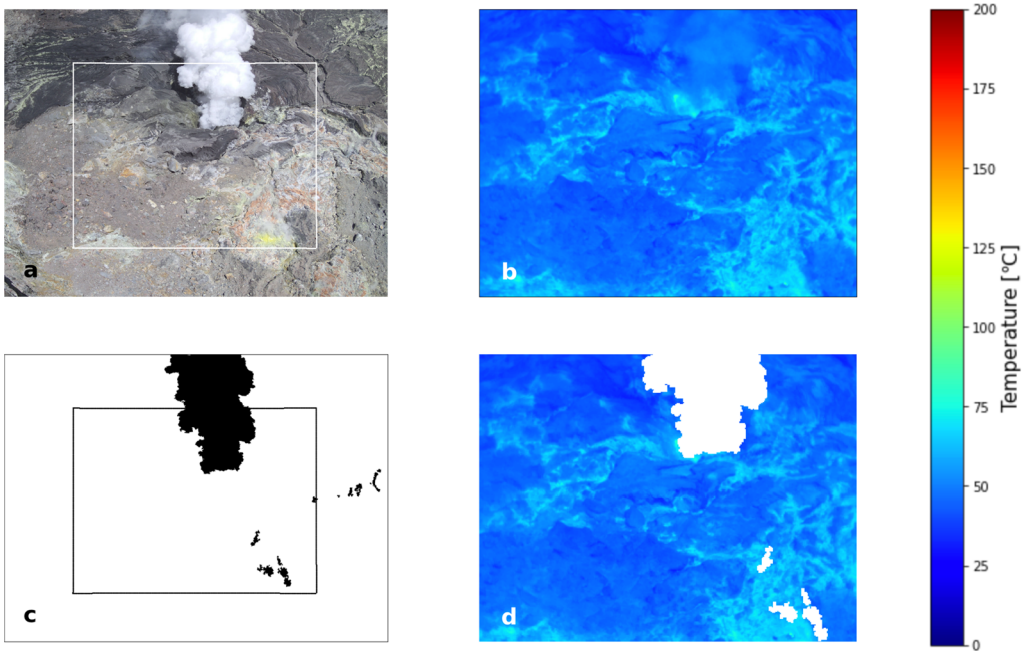

Fig. 1 Image samples acquired with XT2 and used in the masking process. **a** and **b** Visible image of the active crater at Aso volcano in 2020, and its paired TIR image. **c** Area of the condensed vapor on the visible image determined by the software (Agisoft Metashape Professional). **d** TIR image overlapped with the masking image. The white area corresponds to the black area in **c**. The white and black rectangles on **a** and **c** indicate the area corresponding to the TIR image shown in **b**

datasets acquired from the UAV through the SfM–MVS photogrammetric process using commercial software (Agisoft Metashape Professional). Before processing, the portion of the visible images obscured by condensed vapor (white steam) was removed with masking images (Fig. 1c, d) because it could result in spurious surfaces in the resultant DEM. The software yielded dense point clouds with a mean point density of 200 pts/m^2 (Additional file 1: Fig. S5), and we created DEMs with 1 m resolution through interpolation. Although we chose

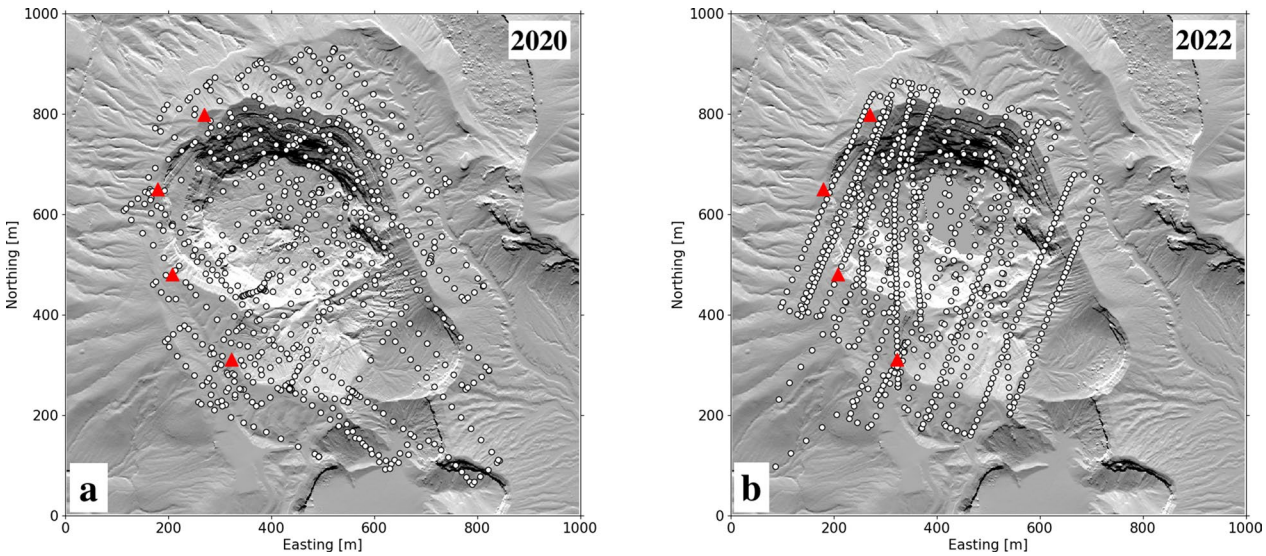

Fig. 2 UAV camera positions for the **a** 2020 and **b** 2022 surveys. The background topography is the DEM created in this study. The white open circles are the camera positions. The red triangles indicate the positions of the GCPs

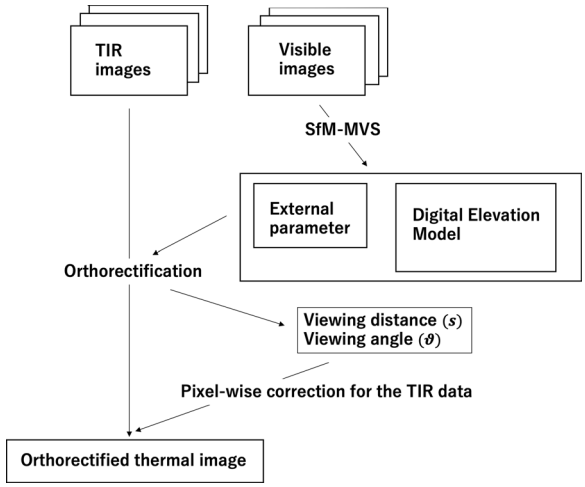

Fig. 3 Workflow of the proposed method SfM–MVS is applied to the visible images to generate DEM. Exterior parameters are estimated in the SfM–MVS at the same time. The TIR images are orthorectified using the DEM and exterior parameters. Through orthorectification, the viewing distance and angle can be obtained for each pixel. These parameters are used to perform a pixelwise correction of the TIR images

four shelter buildings around the crater as ground control points, they were insufficient and not homogeneously distributed (Fig. 2). Therefore, the data obtained outside the crater were somewhat inaccurate (a few meters at some parts; Additional file 1: Fig. S7). We replaced any unsuitable data with the 2012 DEM provided by the Geospatial Information Authority of Japan to create 1-m DEMs of the whole area around the crater (Yokoo et al. 2019). The DEMs for the 2020 and 2022 surveys are shown in Fig. 2 in hillshading.

SfM–MVS provides not only DEMs but also certain optical parameters of the camera and external parameters of each shot, which are necessary for the georeferencing process described in the following section. The optical parameters allow conversion from the pixel coordinate system (2D Cartesian coordinate system that defines the locations of pixels in images) to the image coordinate system (3D Cartesian coordinate system fixed to the camera and reference locations in a film plane; Fig. 4). They consist of focal length f (in pixel units), offset of principal point (c_x, c_y), and lens distortion parameters (k_1, k_2, k_3, p_1, p_2). The optical parameters of the visible cameras were estimated during the DEM creation process described above. The optical parameters of the TIR cameras were also estimated by applying SfM–MVS to TIR images of a target object with thermally distinctive features (our laboratory building). The internal parameters of both visible and TIR cameras are listed in Table 1. External parameters, which

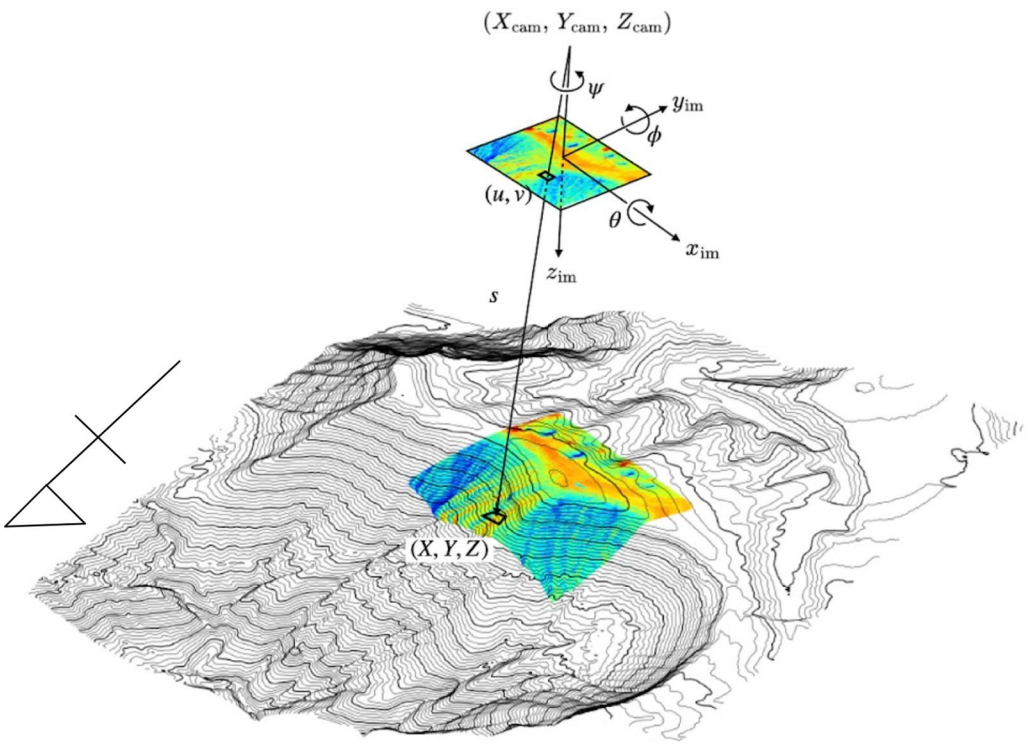

Fig. 4 Schematic illustration of the georeferencing process The TIR image is overlaid onto the DEM surface by converting the pixel coordinate (u, v) into the world coordinate (X, Y, Z). External parameters are also indicated

consist of camera position ($X_{\mathrm{cam}}, Y_{\mathrm{cam}}, Z_{\mathrm{cam}}$) and orientation ($\phi, \theta, \psi$) for each shot, allow the 3D transformation of the image coordinate to the world coordinate (Fig. 4).

We georeferenced the TIR images through direct georeferencing, a technique to orthorectify images with a DEM and external parameter data (Correia et al. 2022). Direct georeferencing aims to convert every pixel coordinate in images (u, v) into the corresponding world coordinate, (X, Y, Z). We assumed that the offset between the center of the TIR image and the corresponding visible image is negligible. As a preparatory step of georeferencing, the effect of lens distortion was corrected with the distortion parameters. After this step, the pixel coordinate was converted by applying the following equations:

$$\nu = \mathbf{R}_{\mathrm{z}}(\psi)\mathbf{R}_{\mathrm{x}}(\phi)\mathbf{R}_{\mathrm{y}}(\theta)\begin{pmatrix}\frac{u-c_{\mathrm{x}}-0.5w}{f}\\ \frac{v-c_{\mathrm{y}}-0.5h}{f}\end{pmatrix}, \quad \text{and} \tag{1}$$

$$\begin{pmatrix}X\\Y\\Z\end{pmatrix} = \begin{pmatrix}X_{\mathrm{cam}}\\Y_{\mathrm{cam}}\\Z_{\mathrm{cam}}\end{pmatrix} + s\frac{\nu}{|\nu|}. \tag{2}$$

In Eq. (1), $\mathbf{R}_{\mathrm{x}}(\phi)$, $\mathbf{R}_{\mathrm{y}}(\theta)$, and $\mathbf{R}_{\mathrm{z}}(\psi)$ are 3×3 rotational matrices around the x, y and z axes of the image coordinate (Fig. 3), and w and h are the width and height, respectively, of the TIR images ((w, h) =(360, 256) for the 2020 survey and (640, 512) for the 2022 survey). In Eqs. (1) and (2), ν is a vector that passes through (u, v) and points toward (X, Y, Z), and s is the viewing distance. The right-hand side of Eq. (2) represents a vector with length s, and it points from ($X_{\mathrm{cam}}, Y_{\mathrm{cam}}, Z_{\mathrm{cam}}$) to ($X$, Y, Z) in world coordinates. The vector was extended until it intersected the DEM surface. Then, the viewing distance s was determined as the length between ($X_{\mathrm{cam}}, Y_{\mathrm{cam}}, Z_{\mathrm{cam}}$) and the intersection (Fig. 4).

Table 1 Optical parameters of FLIR Zenmuse XT2

		XT2[a]		XT2[b]	
		Visible	TIR	Visible	TIR
Focal length	f	4.109e3	5.467e2	4.086e3	7.844e2
Principal point offset	c_{x}	1.408e1	0.0	1.104e1	1.616e0
	c_{y}	2.391e1	0.0	2.594e1	−5.610e0
Distortion parameter	k_1	−4.215e−1	−4.461e−1	−4.166e−1	−3.291e−2
	k_2	2.523e−1	1.987e−1	2.435e−1	1.799e−1
	k_3	−1.127e−1	0.0	−1.062e−1	8.342e−1
	p_1	−6.490e−5	−1.820e−3	8.470e−4	8.364e−5
	p_2	−8.890e−5	−1.106e−3	7.611e−4	−1.252e−3

[a] The XT2 model, whose focus length is 9 mm used for the 2020 survey

[b] The XT2 model, whose focus length is 13 mm used for the 2022 survey

Next, we performed correction to the TIR data. First, the areas of visible condensed vapor in the TIR images were removed with the masking images used in the DEM creation process. The masking images were undistorted with the distortion parameters of the visible camera by the same process as that used for the TIR images (Fig. 1d). Then, every pixel coordinate of the TIR images was converted into the pixel coordinate of the visible images by

$$\left(\frac{u-c_{\mathrm{x}}-0.5w}{f}, \frac{v-c_{\mathrm{y}}-0.5h}{f}, 1\right)_{\mathrm{TIR}} = \left(\frac{u-c_{\mathrm{x}}-0.5w}{f}, \frac{v-c_{\mathrm{y}}-0.5h}{f}, 1\right)_{\mathrm{Visible}}, \tag{3}$$

where subscripts TIR and Visible indicate that the quantity in parentheses is calculated using both the pixel coordinates and optical parameters of TIR and visible images, respectively. Then, every pixel coordinate of the TIR images was associated with the corresponding coordinate of the masking images, which resulted in the coregistration of TIR images and masking images. In this process, we averaged the pixel brightness over the rectangle with its width of $w_{\mathrm{Visible}}/w_{\mathrm{TIR}}$, height of $h_{\mathrm{Visible}}/h_{\mathrm{TIR}}$ and centered around ($u_{\mathrm{Visible}}, v_{\mathrm{Visible}}$). If the average brightness was below a threshold, we considered the temperature datum stored in ($u_{\mathrm{TIR}}, v_{\mathrm{TIR}}$) as affected by condensed water and removed it from the TIR images.

Then, we performed pixelwise TIR data correction for the effects of atmospheric attenuation and emissivity, following Yokoo and Ishii (2021). We extracted the signal strength data stored in the metadata of the TIR images using the ExifTool command. The signal strength by the black body radiation of a target object S_{obj} was calculated from the extracted signal S_{sensor} (Minkina and Dudzik 2009):

$$S_{\mathrm{sensor}} = \tau_{\mathrm{air}}\varepsilon_{\mathrm{obj}}S_{\mathrm{obj}} + (1-\tau_{\mathrm{air}}\varepsilon_{\mathrm{obj}})S_{\mathrm{air}}, \tag{4}$$

where τ_{air} is the transmissivity of the air and $\varepsilon_{\mathrm{obj}}$ is the emissivity of the target object. S_{air} is the signal strength from the thermal radiation of the air and is calculated following Minkina and Dudzik (2009). The transmissivity τ_{air} was calculated using the viewing distance s obtained through the georeferencing process, as well as the relative humidity and atmospheric temperature obtained by vertically extrapolating the records of the neighborhood weather stations operated by the Japan Meteorological Agency (Stations Kumamoto for relative humidity and Otohime for atmospheric temperature, respectively; 30 km SW and 8 km NW from the crater). At the weather stations, the relative humidity was 57.0% and 37.0%, and the atmospheric temperature was 30.2°C and 19.8°C during the 2020 and 2022 surveys, respectively. The data at the stations were extrapolated to the altitude of the

center of the optical paths using the vertical humidity profile of Arikawa and Rokugawa (1995) and the vertical temperature gradient of the air (0.0065 °C/m).

The emissivity ε_{obj} is expressed as $\varepsilon_{obj} = \varepsilon_0 \kappa$, where ε_0 and κ are the intrinsic emissivity toward nadir and a coefficient dependent on the viewing angle (Ball and Pinkerton 2006). We set ε_0 to 0.97 (Mia et al. 2017). The viewing angle was obtained for each pixel by calculating the angle between ν and the normal vector at its corresponding DEM surface. With τ_{air} and ε_{obj}, we calculated S_{obj} by Eq. (4) and then converted it into surface temperature using the conversion formula of Minkina and Dudzik (2009).

After the conversion using Eqs. (1) and (2), the pixel-wise correction for the TIR data was performed, and we averaged the temperature data of the pixels located in the same grid of the DEM. If pixels from two or more TIR images fell onto the same grid, the temperatures of those pixels with shorter viewing distances were preferentially selected as the representative temperature of the grid. In this way, we could minimize the orthorectification error that arises from large viewing angles.

Results and discussion

Orthorectified thermal images in 2020 and 2022

We succeeded in creating two orthorectified thermal images of the active crater at Aso volcano (Figs. 5 and 6). The two orthorectified thermal images were created using two TIR image datasets with different resolutions, which may potentially cause the mixed-pixel effect (Harris 2009) and make it difficult to compare the two images. However, we averaged the temperature data projected onto the DEM in a 1-m size grid (larger than the GSD) in both 2020 and 2022 situations, which can cancel the effect. The image on 18 August 2020 (Figs. 5a and 6a) clearly shows several thermal features in the crater. The south crater wall exhibits a high-temperature area (<200°C) corresponding to a fumarolic field (I in Fig. 6a; the south wall fumarolic field, Yokoo and Ishii 2021). The hot spot at the center of the crater (120°C) is a degassing vent that appeared in May 2019 (Fig. 6a). Areas of relatively hot ground (60°C; II in Fig. 6a) are scattered on both the crater floor and southwest crater wall. They consist of clusters of small degassing vents and small-scale steaming grounds. Figures 5b and 6b show the orthorectified thermal image on 16 March 2022. There is a high-temperature area (<376°C; I in Fig. 6b) on the south wall of the crater in both 2022 and 2020. The hot areas on the crater floor and southwest wall in 2020 (II in Fig. 6a) are barely perceptible on the southwest crater wall in 2022 (50 °C; II in Fig. 6b). The other striking feature of the 2022 image is a volcanic lake with a temperature of 72°C that occupies most of the crater floor (1.1×10^4 m^2). It emerged in the pits created by the two phreatic explosions on 14 and 20 October 2021. The high-temperature spots (180°C) at the northern margin of the lake are degassing vents.

To evaluate the changes in surface temperature, we defined thermally anomalous areas using the statistical method proposed by Kagiyama et al. (1979). First, they fitted the Gaussian curve to the frequency distribution of the target area and calculated its mean and standard deviation(T_0 and σ_T). Then, they defined a thermally anomalous area where the surface temperature is above $T_0 + 3\sigma_T$. In the curve fitting, we used the data of the entire area of the orthorectified thermal images (5.3×10^5 and 4.5×10^5 m^2 in 2020 and 2022, respectively), except for the portion of the volcanic lake. The mean temperature T_0 and standard deviation σ_T were 49.8 and 7.88°C

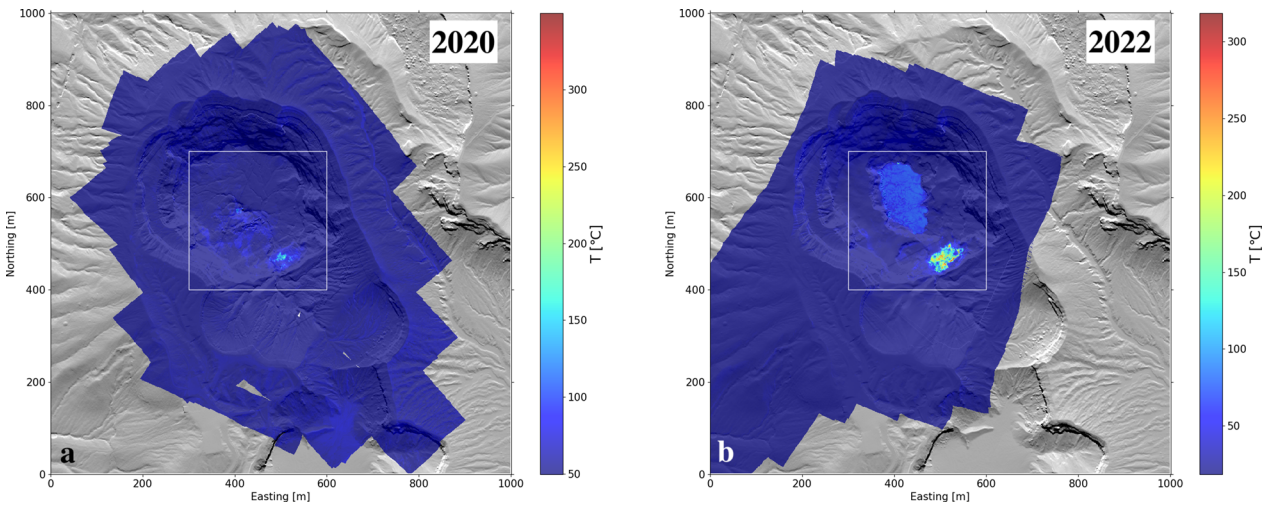

Fig. 5 Orthorectified thermal images of **a** 2020 and **b** 2022 surveys. The white rectangles correspond to the area of Fig. 6c and d

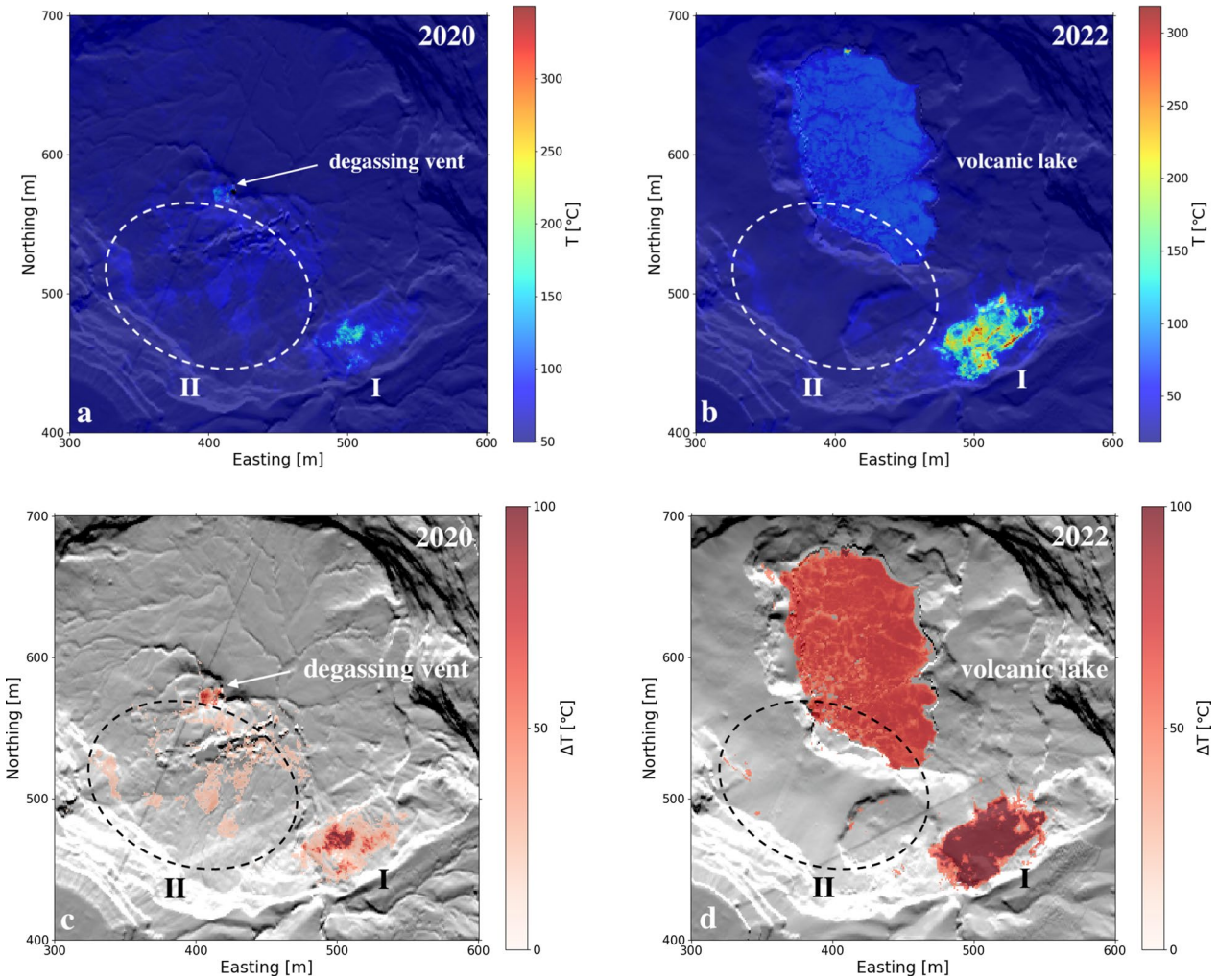

Fig. 6 Orthorectified thermal images zoomed in on the first crater (**a** 2020 survey and **b** 2022 survey) and thermal anomalies (**c** 2020 and **d** 2022). Both maps **a** and **b** show a high-temperature fumarolic field on the south crater wall (I) and steaming grounds scattered on the crater floor and southwest wall (II)

in 2020 and 18.5 and 6.13°C in 2022, respectively. The unnaturally high T_0 in 2020 is likely to reflect intense solar heating and TIR wave reflection. Therefore, we decided to use $\Delta T (= T - T_0)$ to neutralize these effects and evaluate changes of purely volcanic origin. Thermally anomalous areas were determined for the 2020 and 2022 images (Fig. 6c, d). There is clear intensification and extension of the south wall fumarolic field between 2020 and 2022 (200°C to 376°C, 2011 m^2 to 3236 m^2).

Heat discharge rate from the crater

To quantitatively evaluate thermal activities of volcanoes, the heat discharge rate must be calculated, which allows us to compare the magnitude of different forms of heat discharge or quantify temporal changes in a single thermal feature. There are three different forms of heat discharge in the crater: degassing vents, steaming grounds, and a volcanic lake. We calculated the heat discharge rate from the steaming grounds and the volcanic lake using orthorectified thermal images of the crater at Aso volcano.

The heat discharge rate from the fumarolic fields was calculated from the heat balance method proposed by Sekioka and Yuhara (1974):

$$Q_s = K \sum_{T > T_0 + 3\sigma_T} \Delta T A_{grid}, \tag{5}$$

where Q_s is the heat discharge rate in W and K is a constant pertaining to micrometeorological parameters, such as the air temperature, humidity, wind speed, and incident radiation on the ground surface. K is set to 33–50 W m^{-2} K^{-1} following Yokoo and Ishii (2021).

A_{grid} is the area of the DEM grid. The summation indicates that ΔTA_{grid} is integrated over thermally anomalous areas. A_{grid} was calculated by dividing the grid size (1 m^2 for this study) by the vertical component of the normal vector at the grid. Note that we cannot quantify the heat discharge rate of degassing vents scattered on the south wall fumarolic field (I in Fig. 6a) and the crater floor and southwest wall (II in Fig. 6b) by Eq. (5). In 2020, the heat discharge rate from each steaming ground was 2.6–4.0 MW (I), 2.6–4.0 MW (II), and 5.2–8.0 MW in total. That of 2022 was 14–21 MW (I), 0.23–0.36 MW (II), and 14–21 MW in total (Table 2). The heat discharge rate of the south wall fumarolic field showed a sevenfold increase during 2020–2022. The activation of this fumarolic field is probably related to the change in the underlying hydrothermal or fracture system accompanying the phreatic explosions on 14 and 20 October 2021. The heat discharge rate from the south wall fumarolic field in August 2020 was an order of magnitude larger than the value reported in a previous study (0.2–0.3 MW; Yokoo and Ishii, 2021). This discrepancy is attributed to the area where T_0 and σ_T were calculated (reference area; 5.3×10^5 m^2 in this study and 5,500 m^2 in Yokoo and Ishii, 2021). As noted in Kagiyama et al. (1979) and Kagiyama and Hagiwara (1981), curve fitting yields reliable results only when the reference area is sufficiently extensive compared to the area of the target thermal anomaly. We hypothesize that the reference area of 5,500 m^2 was insufficient compared to the area of the south wall fumarolic field(~2,000 m^2). As we increased the reference area from 5,500 m^2 to 5.3×10^5 m^2, T_0 and σ_T decreased until they converged into constant values at 2.2×10^5 m^2. The heat discharge rate increased from 0.74–1.1 MW to 2.6–4.0 MW with the increase in the reference area and remained constant when the reference area was larger than 2.2×10^5 m^2 (Fig. 7). This observation supports our speculation and validates our choice of the reference area.

The heat discharge rate from the volcanic lake was calculated following Terada et al. (2012). The heat discharge rate from the lake surface (Q_l) is calculated by

$$Q_l = (\phi_e + \phi_c + \phi_r)S \quad (6)$$

where ϕ_e, ϕ_c, and ϕ_r are heat fluxes from evaporation, conduction, and radiation, respectively, and S is the lake's surface area. The heat flux from evaporation ϕ_e depends on three factors: temperature of the air directly above the lake, ambient air temperature, and wind speed at the lake surface. The first and second factors were substituted by the lake surface temperature (72°C) and the temperature at the crater rim, respectively. The third factor, wind speed, was calculated using a motion tracking algorithm

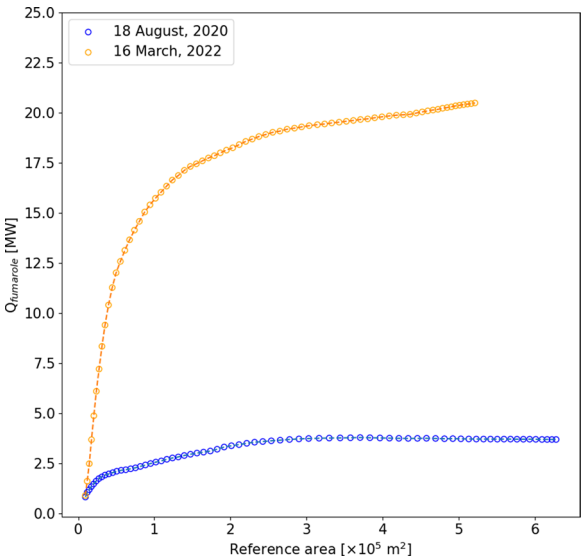

Fig. 7 Relation between the reference area and heat discharge rate. The heat discharge rate converges as the reference area increases

Table 2 Heat discharge rate from the crater at Aso volcano

Date	Steaming ground [MW]		Volcanic lake [MW]	Total [MW]
	I[a]	II[b]		
August 2020	2.6-4.0	2.4-3.6	-	5.2-8.0
March 2022	14-21	0.23-0.36	58-73	72-94

[a] The south wall fumarolic field

[b] The steaming ground on the crater floor and southwest wall

for the time-series images of the steam above the lake. The wind speed was estimated to be 0.9–2.7 m/s. We calculated the heat discharge fluxes from conduction ϕ_c and radiation ϕ_r after Terada et al. (2012) using Bowen's relationship and the Stefan–Boltzmann formula, respectively. The total heat discharge rate from the lake was estimated to be 58–73 MW (Table 2). The heat discharge rate from the volcanic lake was 3–5 times larger than that from the steaming grounds in 2022 (Table 2). Several studies have calculated the heat discharge rate from the crater lake: 60–100 MW (1981–1984; Fukui 1995) and 150–200 MW (2000–2003; Saito et al. 2008), and 200 MW (2006–2009; Terada et al. 2012). Our estimate is close to the value in 1981–1984 and significantly smaller than the values in 2000–2003 and 2006–2009. In 2000–2003 and 2006–2009, the surface area of the lake was 4–5 times larger than in 2022, which explains the gap in heat discharge between 2006–2009 and 2022.

Conclusions

We propose a simple TIR data processing method to reconstruct the 3D ground surface temperature field of volcanoes, incorporating pixelwise correction for atmospheric attenuation and emissivity. We demonstrated our method at the active crater at Aso volcano. The orthorectified thermal images created by our method in August 2020 and March 2022 showed evident changes in the thermal state of the crater. To quantitatively compare the magnitude of the different forms of thermal activity and evaluate the changes during the period, we calculated the heat discharge rates from the steaming grounds and the volcanic lake. The heat discharge rate from the volcanic lake was 3–5 times larger than that from the steaming grounds. The heat discharge rate from the fumarolic field on the south crater wall showed a sevenfold increase after the phreatic explosions on 14 and 20 October 2021. We were not able to evaluate the heat discharge rate from degassing vents, which is essential to fully discuss the thermal state of the volcano. The plume rise method (Kagiyama 1981) or other methods (Gaudin et al. 2016; Jinguji and Ehara 1996) could be used to obtain these values.

Abbreviations

TIR: Thermal Infrared
UAV: Unoccupied aerial vehicle
DEM: Digital elevation model
SfM–MVS: Structure from Motion–Multi-view Stereo

Supplementary Information

The online version contains supplementary material available at https://doi.org/10.1186/s40623-023-01786-8.

Additional file 1: Fig. S1. Estimation of the difference in temperature data resulting from the different temperature correction strategies in the case of an oblique camera pose. **Fig. S2.** Estimation of the difference in temperature data resulting from the different temperature correction strategies in the case of an oblique camera pose. **Fig. S3.** Estimation of the difference in temperature data resulting from the different temperature correction strategies in the case of a vertical camera pose. **Fig. S4.** Geographic setting of Aso volcano. **Fig. S5.** Point cloud density map of the 2020 (a) and 2022 (b) surveys. **Fig. S6.** Orthoimages of the active crater of Aso volcano. **Fig. S7**. Estimation of the error of the DEMs.

Acknowledgements

We thank all staff members of the Aso Volcanological Laboratory for their support. T. Nishimura kindly provided the XT2 for the 2022 survey. The Aso Volcano Disaster Prevention Council supported our surveys at the volcano. We also thank to Alessandro Fornaciai and an anonymous reviewer for helpful comments and suggestions that have greatly improved the manuscript. The editor, Sonia Calvari, gave us helpful feedback.

Author contributions

SN performed all analysis except for the DEM creation and wrote the manuscript. AY performed data acquisition and the DEM creation. NS and AY contributed to the planning and interpretation of this study. All authors read and approved the final manuscript.

Funding

This study was financially supported by the Ministry of Education, Culture, Sports, Science and Technology of Japan under its Earthquake and Volcano Hazards Observation and Research Program, JSPS KAKENHI Grant Number 19K03992, and ISHIZUE 2022 of Kyoto University.

Availability of data and materials

The datasets used and/or analyzed during the current study are available from the corresponding author on reasonable request.

Declarations

Competing interests

The authors declare that they have no competing interests.

Author details

[1]Graduate School of Science, Kyoto University, Kyoto 606-8502, Japan. [2]Aso Volcanological Laboratory, Institute for Geothermal Sciences, Graduate School of Science, Kyoto University, Aso, Japan.

Received: 12 September 2022 Accepted: 15 February 2023
Published online: 18 April 2023

References

Arikawa T, Rokugawa S (1995) Derivation of Japan model atmospheres from Rawinsonde data influence of water vapor content profiles on atmospheric correction for ASTER TIR data. J Remote Sens Soc Jpn 15:198–211. https://doi.org/10.11440/rssj1981.15.198

Ball M, Pinkerton H (2006) Factors affecting the accuracy of thermal imaging cameras. J Geophys Res 111:B11203. https://doi.org/10.1029/2005JB003829

Bonaccorso P, Calvari S, Carfi G, Lodato L, Patané D (2003) December 2002 flank failure and Tsunami at Stromboli volcano inferred by volcanological and geophysical observations. Geophys Res Lett 30:1941–1944. https://doi.org/10.1029/2003GL017702

Chiodini G, Vilardo G, Augusti V, Granieri D, Caliro S, Minopoli C, Terranova C (2007) Thermal monitoring of hydrothermal activity by permanent infrared automatic stations: results obtained at Solfatara di Pozzuoli, Campi Flegrei (Italy). J Geophys Res 112:B12206. https://doi.org/10.1029/2007JB005140

Correia CAM, Andrade FAA, Silverton A, Guedes IP, Pinto MF, Manhães AG, Haddad DB (2022) Comprehensive direct georeferencing of aerial images for unmanned aerial systems applications. Sensors 22(2):604. https://doi.org/10.3390/s22020604

Fornaciai A, Andronico D, Favalli M, Spampinato L, Branca S, Lodato L, Bonforte A, Nannipieri L (2021) The 2004–2005 Mt. Etna compound Lava Flow Field: A Retrospective Analysis by combining remote and Field Methods. J Geophys Res 126:e2020JB020499. https://doi.org/10.1029/2020JB020499

Fukui K (1995) H2O and heat discharged from Aso volcano in noneruptive stage. Bull Volcanol Soc Jpn 40:233–248. https://doi.org/10.18940/kazan.40.4_233

Gaudin D, Beauducel F, Allemand P, Delacourt C, Finizola A (2013) Heat flux measurement from thermal infrared imagery in low-flux fumarolic zones: example of the Ty fault (La Soufriére de Guadeloupe). J Volcanol Geotherm Res 267:47–56. https://doi.org/10.1016/j.jvolgeores.2013.09.009

Gaudin D, Beauducel F, Countant O, Delacourt C, Richon P, de-Chabalier JB, Hammouya G (2016) Mass and heat flux balance of La Soufriére volcano (Guadeloupe) from aerial infrared thermal imaging. J Volcanol Geotherm Res 320:107–116. https://doi.org/10.1016/j.jvolgeores.2016.04.007

Harris A (2009) Thermal remote sensing of active volcanoes: a user's manual. Cambridge University Press, UK, pp 155–157p

James MR, Robson S, Pinkerton H, Ball M (2006) Oblique photogrammetry with visible and thermal images of active lava flows. Bull Volcanol 69(1):105–108. https://doi.org/10.1007/s00445-006-0062-9
Jinguji M, Ehara S (1996) Estimation of steam and heat discharge rates from volcanoes using maximum diameter of volcanic steam. Bull Volcanol Soc Jpn 41(1):23-29. https://doi.org/10.18940/kazan.41.1_23
Kagiyama T, Uhira K, Watanabe T, Masutani F, Yamaguchi M (1979) Geothermal survey of volcanoes Kirishima. Bull Earthq Res Inst 54:187–210
Kagiyama T, Hagiwara M (1981) Geothermal survey in and around O-ana Crater and Jodo-daira Flat, the Volcanoes Azuma. Bull Earthq Res Inst 55:681–703
Kagiyama T (1981) Evaluation methods of heat discharge and their applications to the major active volcanoes in Japan. J Volcanol Geotherm Res 9:87–97. https://doi.org/10.1016/0377-0273(81)90016-0
Lewis A, Hilley GE, Lewicki JL (2015) Integrated thermal infrared imaging and structure-from-motion photogrammetry to map apparent temperature and radiant hydrothermal heat flux at Mammoth Mountain, CA, USA. J Volcanol Geotherm Res 303:16–24. https://doi.org/10.1016/j.jvolgeores.2015.07.025
Lewis A, Sare R, Lewicki JL, Hilley GE (2020) High-resolution imaging of hydrothermal heat flux using optical and thermal structure-from-motion photogrammetry. J Volcanol Geotherm Res 393:106818. https://doi.org/10.1016/j.jvolgeores.2020.106818
Matsushima N, Kazahaya K, Saito G, Shinohara H (2003) Mass and heat flux of volcanic gas discharging from the summit crater of Iwodake volcano, Satsuma-Iwojima, Japan, during 1996–1999. J Volcanol Geotherm Res 126:285–301. https://doi.org/10.1016/S0377-0273(03)00152-5
Mia MB, Fujimitsu Y, Nishijima J (2017) Thermal activity monitoring of an active volcano using landsat 8/OLI-TIRS sensor images: a case study at the Aso volcanic area in Southwest Japan. Geosciences. 7(4):118. https://doi.org/10.3390/geosciences7040118
Minkina W, Dudzik S (2009) Infrared thermography: errors and uncertainties. Wiley, UK, 192p
Miyabuchi Y, Iizuka Y, Ennyu F, Ohkura T (2021) Precursor activity of the 2019–2020 magmatic eruption at Nakadake first crater, Aso volcano: insights from Ash Fall deposits from early activity on May 3–5, 2019. Bull Volcanol Soc Jpn 66:157–169. https://doi.org/10.18940/kazan.66.3_157
Saito T, Ohsawa S, Hashimoto T, Terada A, Yoshikawa S, Ohkura T (2008) Water, heat and chloride balances of the crater lake at Aso volcano, Japan. J Geotherm Res Soc Jpn 30:107–120. https://doi.org/10.11367/grsj1979.30.107
Sawyer GM, Burton MR (2006) Effects of a volcanic plume on thermal imaging data. Geophys Res Lett 33:L14311. https://doi.org/10.1029/2005GL025320
Sekioka M, Yuhara K (1974) Heat flux estimation in geothermal areas based on the heat balance of the ground surface. J Geophys Res 79:2053–2058. https://doi.org/10.1029/JB079i014p02053
Stevenson JA, Varley N (2008) Fumarole monitoring with a handheld infrared camera: Volcán de Colima, Mexico, 2006–2007. J Volcanol Geotherm Res 177:911–924. https://doi.org/10.1016/j.jvolgeores.2008.07.003
Sudo Y, Tsutsui T, Nakaboh M, Yoshikawa M, Yoshikawa S, Inoue H (2006) Ground deformation and magma reservoir at Aso volcano: location of deflation source derived from long-term geodetic surveys. Bull Volcanol Soc Jpn 51:291–309. https://doi.org/10.18940/kazan.51.5_291
Terada A, Hashimoto T, Kagiyama T (2012) A water flow model of the active crater lake at Aso volcano, Japan: fluctuations of magmatic gas and ground water fluxes from the underlying hydrothermal system. Bull Volcanol 74:641–655. https://doi.org/10.1007/s00445-011-0550-4
Thiele S, Varley N, James M (2017) Thermal photogrammetric imaging: a new technique for monitoring dome eruptions. J Volcanol Geotherm Res 337:40–145. https://doi.org/10.1016/j.jvolgeores.2017.03.022
Vaughan RG, Hook SJ, Ramsey MS, Realmuto DJ, Schneider DJ (2005) Monitoring eruptive activity at Mount. St. Helens with TIR image data. Geophys Res Lett 32:L19305. https://doi.org/10.1029/2005GL024112
Yokoo A, Ishii K, Ohkura T, Kim K (2019) Monochromatic infrasound waves observed during the 2014–2015 eruption of Aso volcano, Japan. Earth Planets Space 71:12. https://doi.org/10.1186/s40623-019-0993-y
Yokoo A, Ishii K (2021) Process to analyze radiometric JPEG files taken by a thermal infrared camera. Bull Volcanol Soc Jpn 66:229–240. https://doi.org/10.18940/kazan.66.3_229

Publisher's Note